Plaquette ordered phase and quantum spin liquid in the spin-$\frac{1}{2}$ J_1-J_2 square Heisenberg model

Shou-Shu Gong[1], Wei Zhu[1], D. N. Sheng[1], Olexei I. Motrunich[2], Matthew P. A. Fisher[3]
[1]*Department of Physics and Astronomy, California State University, Northridge, California 91330, USA*
[2]*Department of Physics, California Institute of Technology, Pasadena, California 91125, USA*
[3]*Department of Physics, University of California, Santa Barbara, California 93106-9530, USA*

We study the spin-$\frac{1}{2}$ Heisenberg model on the square lattice with first- and second-neighbor antiferromagnetic interactions J_1 and J_2, which possesses a nonmagnetic region that has been debated for many years and might realize the interesting Z_2 spin liquid (SL). We use the density matrix renormalization group approach with explicit implementation of $SU(2)$ spin rotation symmetry and study the model accurately on open cylinders with different boundary conditions. With increasing J_2, we find a Néel phase, a plaquette valence-bond (PVB) phase with a finite spin gap, and a possible spin liquid in a small region of J_2 between these two phases. From the finite-size scaling of the magnetic order parameter, we estimate that the Néel order vanishes at $J_2/J_1 \simeq 0.44$. For $0.5 < J_2/J_1 < 0.61$, we find dimer correlations and PVB textures whose decay lengths grow strongly with increasing system width, consistent with a long-range PVB order in the two-dimensional limit. The dimer-dimer correlations reveal the s-wave character of the PVB order. For $0.44 < J_2/J_1 < 0.5$, both spin order, dimer order, and spin gap are small on finite-size systems and appear to scale to zero with increasing system width, which is consistent with a possible gapless SL or a near-critical behavior. We compare and contrast our results with earlier numerical studies.

PACS numbers: 73.43.Nq, 75.10.Jm, 75.10.Kt

Introduction.—Quantum spin liquid (SL) is an exotic state of matter where a spin system does not form magnetically ordered state or break lattice symmetries even at zero temperature[1]. Understanding spin liquids is important in frustrated magnetic systems and may also hold clues to understand non-Fermi liquid of doped Mott materials and high-T_c superconductivity of strongly correlated systems[2]. The exciting properties of spin liquids such as deconfined quasiparticles and fractional statistics have been revealed in many artificially constructed systems such as quantum dimer models[3–5], Kagome spin model in the easy axis limit[6–10], and Kitaev model[11]. The possibility of finding spin liquids in realistic Heisenberg models, which may be close to experimental materials, has attracted much attention of the field over the last twenty years. The prominent example is the Kagome antiferromagnet, where recent density matrix renormalization group (DMRG) studies point to a gapped Z_2 SL[10, 12–15] characterized by a Z_2 topological order and fractionalized spinon and vison excitations[16–20].

One of the simplest candidate Heisenberg models for SL is the spin-$\frac{1}{2}$ J_1-J_2 square lattice model. The Hamiltonian is

$$H = J_1 \sum_{\langle i,j \rangle} S_i \cdot S_j + J_2 \sum_{\langle\langle i,j \rangle\rangle} S_i \cdot S_j \ , \qquad (1)$$

where the sums $\langle i,j \rangle$ and $\langle\langle i,j \rangle\rangle$ run over all the nearest-neighbor (NN) and the next nearest-neighbor (NNN) bonds, respectively. We set $J_1 = 1$ as energy scale. The frustrating J_2 couplings suppress the Néel order and induce a nonmagnetic region around the strongest frustration point $J_2 = 0.5$, which has been studied extensively[21–42]. Different candidate states have been proposed based on various approximate methods or small-size exact diagonalization calculations, such as plaquette valence-bond (PVB) state[23, 26, 29, 30, 32, 35, 42], columnar valence-bond (CVB) state[21, 22, 25], or gapless SL[27, 28, 40, 41]. However, the true nature of the quantum phase has remained unresolved.

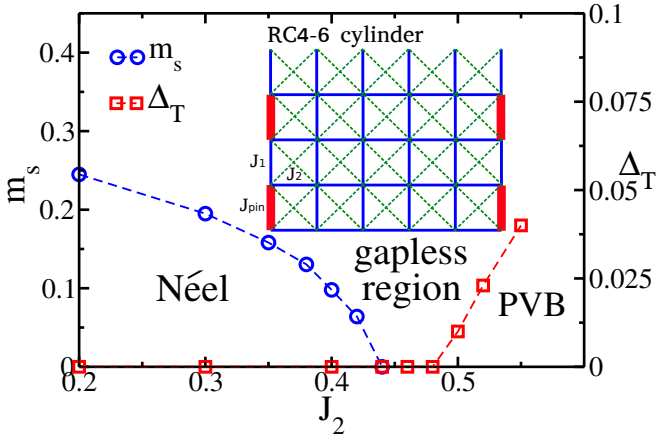

FIG. 1: (color online) Phase diagram of spin-$\frac{1}{2}$ J_1-J_2 square Heisenberg model for $J_2 < 0.61$ obtained by our $SU(2)$ DMRG studies. With growing J_2, the model has a Néel phase for $J_2 < 0.44$ and a PVB phase for $0.5 < J_2 < 0.61$. Between these two phases, there is a small gapless region that exhibits no order in our calculations, consistent with a gapless SL. The main panel shows Néel order parameter m_s and spin gap Δ_T in the thermodynamic limit. The inset is a sketch for a RC4-6 cylinder; $J_{\rm pin}$ shows the modified odd vertical NN bonds providing the boundary pinning for dimer orders.

Recent large-scale DMRG study of the J_1-J_2 square lattice model[37] proposed a gapped Z_2 SL for $0.41 \leq J_2 \leq 0.62$ by establishing the absence of the magnetic and dimer orders, by finding nonzero singlet and triplet gaps, and by measuring a positive topological entanglement entropy term close to the value $\gamma = \ln 2$ expected for a Z_2 SL[43, 44]. Very recent VMC work[41] with two steps of Lanczos improvement proposed a gapless Z_2 SL for $0.45 \lesssim J_2 \lesssim 0.6$ with competitive

energies. On the other hand, recent DMRG studies[45–47] of another bipartite frustrated system—the J_1-J_2 spin-1/2 honeycomb lattice Heisenberg model—found a PVB phase in the nonmagnetic region, with a possible SL phase between the Néel and PVB phases[47] or with a direct Néel to PVB transition characterized by a deconfined quantum critical point[45–49]. These studies[46, 47] also found that in the nonmagnetic region the convergence of DMRG in wider systems, which is controlled by the number of states kept, is crucial for determining the true nature of the ground state.

In this Letter, we reexamine the J_1-J_2 square lattice Heisenberg model for $J_2 < 0.61$ using DMRG algorithm with explicit implementation of the $SU(2)$ spin rotation symmetry[50] (we do not study the well known stripe antiferromagnetic phase at larger J_2). We find accurate results on cylinders with system width up to $12 \sim 14$ lattice spacings by keeping as many as 36000 optimal $U(1)$-equivalent states. We find a Néel phase below $J_2 \simeq 0.44$ and a nonmagnetic region for $0.44 < J_2 < 0.61$ by finite-size scaling of the magnetic order parameter. In the nonmagnetic region, we establish a PVB order for $J_2 > 0.5$—in contrast to the previous proposal [37] of a Z_2 SL—by observing that the PVB decay length grows strongly with increasing system width. Some of our findings for the phases in this model had been suggested in Ref. [51]. We identify the PVB order as the s-wave plaquette[30] by studying dimer-dimer correlations. For $0.44 < J_2 < 0.5$, we find that the magnetic order, valence-bond crystal (VBC) orders, as well as spin excitation gap all vanish with increasing system width, which suggest a possible gapless SL in agreement with the VMC results[41] or a near-critical behavior.

We consider both torus and cylinder samples in DMRG calculations, but all the phases are established based on high accuracy results on cylinders[52]. We use two cylinder geometries. The first is the rectangular cylinder (RC) with closed boundary in the y direction and open boundaries in the x direction. Such a system is denoted RCL_y-L_x, where L_y and L_x are number of sites in the y and x directions; the width of the cylinder is $W_y = L_y$. The inset of Fig. 1 shows an RC4-6 cylinder. The RC cylinders preserve translational symmetry in the y direction. If we want to study VBC order with dimers oriented in the y direction, we can induce such an order near the open boundaries by modifying every other NN vertical bond on the boundary to be $J_{\rm pin} \neq J_1$, which is also illustrated in Fig. 1. The second geometry is the tilted cylinder (TC) obtained by cutting cylinder edge along one diagonal direction of the square lattice, as shown below in Fig. 4(a) when discussing the PVB order.

Néel order.—Néel order parameter m_s^2 is defined as $m_s^2 = \frac{1}{N^2}\sum_{i,j}\langle S_i \cdot S_j\rangle e^{i\vec{q}\cdot(\vec{r}_i-\vec{r}_j)}$ (N is the total number of sites) with the antiferromagnetic ordering wave vector $\vec{q} = (\pi, \pi)$. We calculate m_s^2 from the spin correlations of the $L \times L$ sites in the middle of the RCL-2L cylinder, which efficiently reduces boundary effects[37, 53]. In Fig. 2(a), we show m_s^2 for different systems with $L = 4$ to 14[54]. We fit the finite-size data using the polynomial function up to fourth order, which

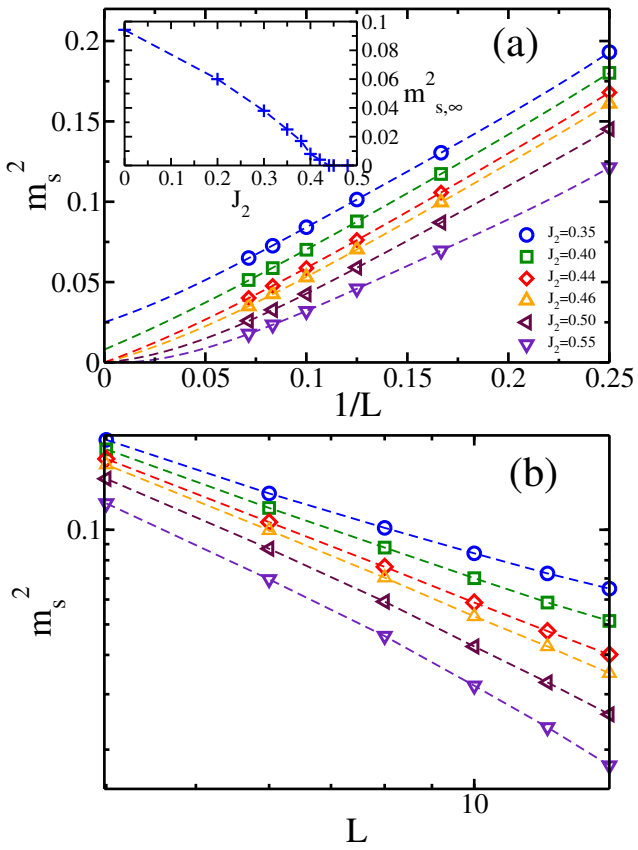

FIG. 2: (color online) (a) m_s^2 plotted vs $1/L$ for RCL-2L cylinder with $L = 4, 6, 8, 10, 12, 14$; lines are polynomial fits up to fourth order. The inset is J_2 dependence of the obtained magnetic order in the 2D limit $m_{s,\infty}^2$. (b) Same data shown as log-log plot of m_s^2 versus width L.

works quite well. The intercept with the vertical axis provides an extrapolation of m_s^2 to the two-dimensional (2D) limit, and we show thus obtained $m_{s,\infty}^2$ in the inset of Fig. 2(a). Such an analysis suggests that the Néel order vanishes for $J_2 > 0.44$.

The estimated critical J_2 of spin order vanishing is different from the point where the PVB order develops as found below. One possibility is an intermediate SL phase. Another possibility is that the system is near critical in the window $0.44 < J_2 < 0.5$. In the latter case, to get some idea about the criticality, Fig. 2(b) shows log-log plot of m_s^2 versus L. m_s^2 approaches finite value in the Néel phase, and we see this developing for $J_2 = 0.35$ and 0.4. On the other hand, we expect $m_s^2(L) \sim L^{-(1+\eta)}$ at a critical point and $m_s^2(L) \sim L^{-2}$ in the nonmagnetic phase. The accelerated decay of $m_s^2(L)$ at $J_2 = 0.55$ is consistent with vanishing Néel order at this point: from the two largest sizes at $J_2 = 0.55$, we estimate $m_s^2(L) \sim L^{-1.82}$, which is quite close to $m_s^2(L) \sim L^{-2}$. In the near-critical region, we can fit the $J_2 = 0.44$ data to $L^{-(1+0.15)}$ and the $J_2 = 0.5$ data for $L > 8$ to $L^{-(1+0.44)}$. This range of η is compatible with the findings in the J-Q models on the square ($\eta \simeq 0.26 - 0.35$)[55–61] and honeycomb ($\eta \simeq 0.3$)[62] lattices, which show continuous Néel to VBC

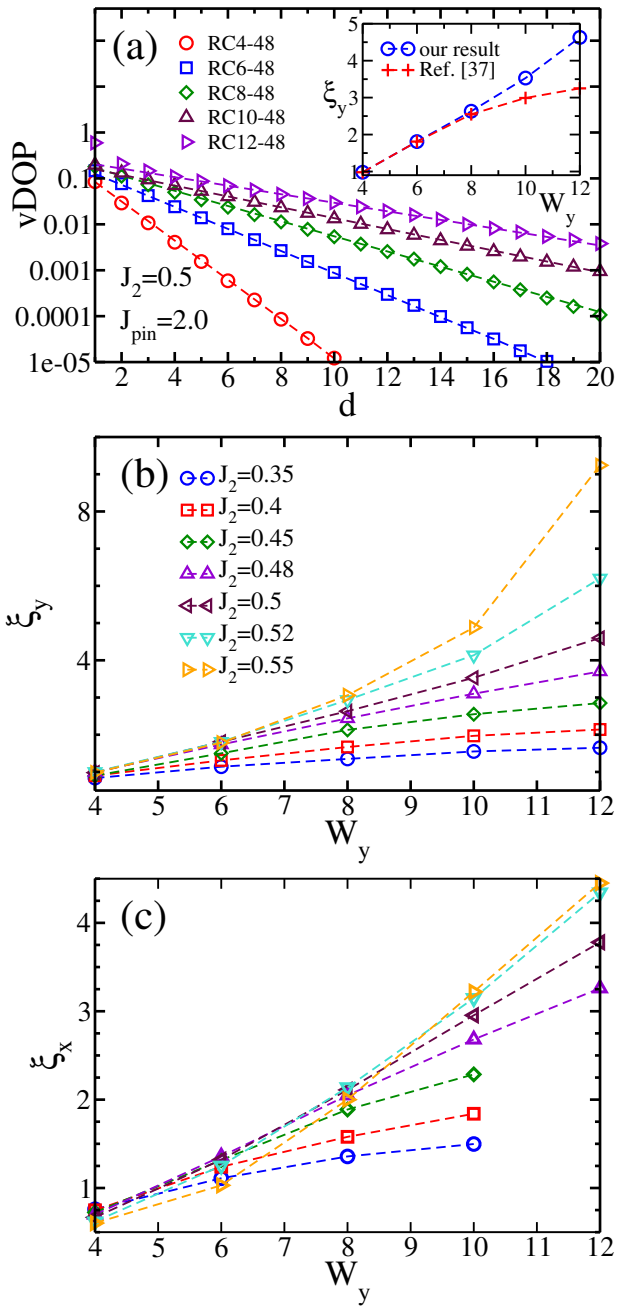

FIG. 3: (color online) (a) Log-linear plot of vDOP for $J_2 = 0.5$ and $J_{\rm pin} = 2.0$ on RC cylinder. The inset is the comparison of width dependence of the vertical dimer decay length $\xi_{\rm y}$ with Ref. [37]. (b) and (c) are $\xi_{\rm y}$ and $\xi_{\rm x}$ versus W_y on RC cylinders with $J_{\rm pin} = 2.0$ for a range of J_2 shown with the same symbols in both panels.

transition argued to be in the deconfined criticality class, so our model is compatible with this scenario as well.

VBC orders.—To investigate the VBC order on cylinder, we introduce the "pinning" bonds $J_{\rm pin} \neq J_1$ on boundaries to induce a vertical dimer pattern, and measure the decay length of the dimer order parameter (DOP) texture from the edge to the middle of cylinder[37, 51]. The vertical DOP (vDOP) for each column is defined as the difference of the strong and weak vertical bond energies. In Fig. 3(a), we show log-linear plot of the vDOP for $J_2 = 0.5$ and $J_{\rm pin} = 2.0$ on long cylinders, which allows us to determine the decay length $\xi_{\rm y}$ by a straight line fitting to the data points. If we take different pinning strength $J_{\rm pin}$ at the boundary, we find that although the amplitude of the vDOP texture changes, the decay length $\xi_{\rm y}$ is independent of $J_{\rm pin}$ (see Suppl. Material). In the inset of Fig. 3(a) we compare our $\xi_{\rm y}$ at $J_2 = 0.5$ with those in Ref. [37]. We observe consistency on small sizes $W_y \leq 8$, but disagreement on large sizes $W_y \geq 10$[63]. The disagreement might originate from less good convergence in Ref. [37]. Our results are fully converged by keeping 16000 (24000) states for $L_y = 10$ (12) systems, and we also find that $\xi_{\rm y}$ is independent of the system length on our studied long cylinders (see Suppl. Material). In Fig. 3(b), we show width dependence of $\xi_{\rm y}$ for various J_2 with $J_{\rm pin} = 2.0$. The $\xi_{\rm y}$ grows slowly and saturates to a constant on wide cylinders for $J_2 < 0.5$, demonstrating the vanishing VBC order. For $J_2 > 0.5$, the $\xi_{\rm y}$ grows faster than linear in W_y, which suggests nonzero vDOP in the 2D limit.

Besides the vertical dimer texture, the system also has the horizontal bond dimer pattern with an exponentially decaying horizontal DOP (hDOP) from the boundary to the bulk. In Fig. 3(c), we find that the hDOP decay length $\xi_{\rm x}$ also grows strongly for $J_2 > 0.5$. Thus our results indicate the nonzero horizontal dimer order coexisting with the vertical dimer order, which suggests that the VBC state has plaquette (PVB) rather than columnar (CVB) order.

We also study the spontaneous nonzero bulk hDOP on RC cylinders with odd L_y[37, 64] (see Suppl. Materials). We find that with increasing L_y, the hDOP drops rapidly to zero for $J_2 < 0.5$, but decreases slowly and possibly approaches a finite value for $J_2 > 0.5$, consistent with a VBC order.

To find if there is a strong tendency of the system towards developing dimer order without using boundary pinning, we study the structure factors $S_{\rm vbc}$ and $S_{\rm col}$ as described in Ref. [30]; the former detects both the PVB and CVB orders while the latter is nonzero only for the CVB order. We take RCL-2L cylinders with no pinning and calculate the structure factors using the dimer-dimer correlations of the $L \times L$ sites in the middle. The picture of the dimer correlations is consistent with the s-wave plaquette state[30] (see Suppl. Material). The finite-size extrapolations of the structure factors show that while $S_{\rm vbc}/N$ possibly approaches finite values for $J_2 > 0.5$, $S_{\rm col}/N$ clearly approaches zero with increasing L_y in the nonmagnetic region, which definitely excludes the CVB order.

To explicitly demonstrate the PVB order, we study cylinders with a different geometry obtained by cutting the cylinder along one diagonal direction of the square lattice and trimming every other site on the boundary as shown in Fig. 4(a). We label such a tilted cylinder as TCL_y-L_x, where L_y and L_x denote number of square plaquettes stacked along their diagonals in the vertical and horizontal direction; the width of the cylinder is $W_y = \sqrt{2}L_y$ in units of NN lattice spacing. The trimmed edges induce strong PVB order on boundaries as can be seen in Fig. 4(a). We denote the sum of the four NN bond

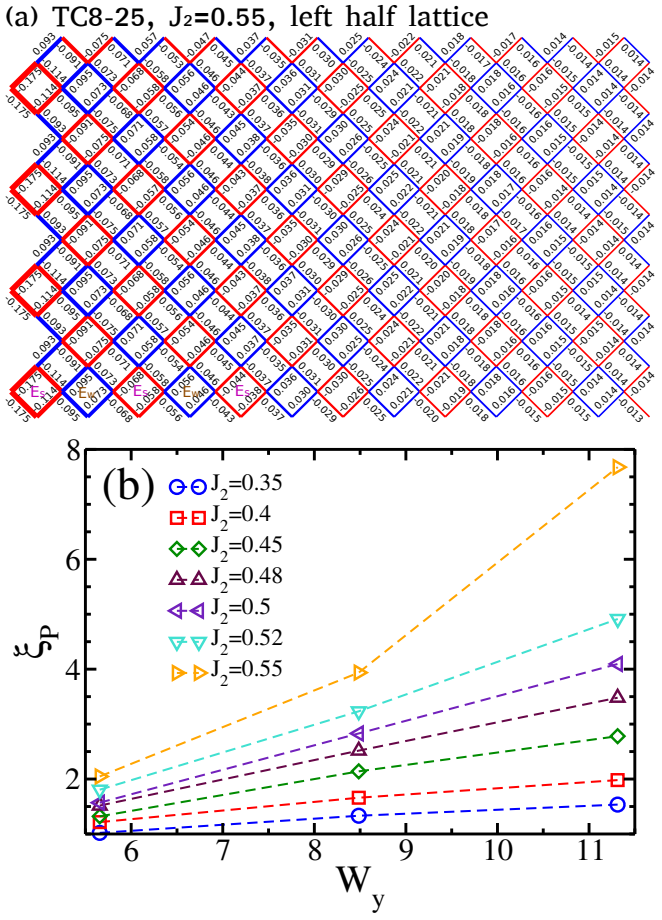

FIG. 4: (color online) (a) NN bond energy for $J_2 = 0.55$ on the left half of TC8-25 cylinder; all the bond energies have subtracted a constant -0.2948. We trim every other site on both boundaries to make lattice select unique PVB order. E_s (E_w) denotes the sum of four NN bond energies of the red (blue) plaquette with negative (positive) numbers. (b) Dependence of the pDOP decay length $\xi_{\rm P}$ on the cylinder width W_y.

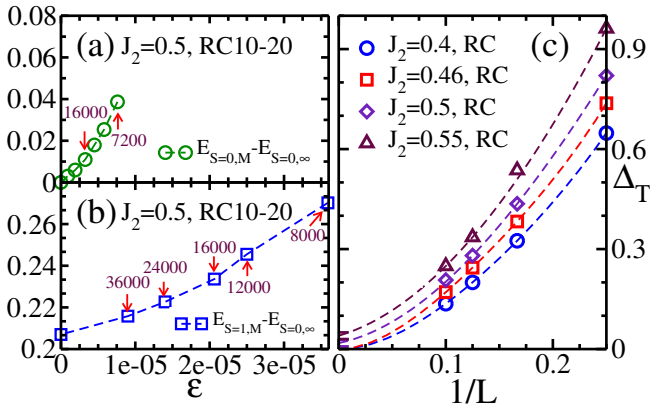

FIG. 5: (color online) (a) and (b) Ground-state energies for RC10-20 cylinder at $J_2 = 0.5$ in the $S = 0$ ($E_{S=0,M}$) and $S = 1$ ($E_{S=1,M}$) sectors vs the DMRG truncation error ε. All the energies have subtracted the ground-state energy $E_{S=0,\infty} = -99.022(1)$. M is the number of kept $U(1)$-equivalent DMRG states and is also indicated next to the symbols. (c) Finite-size extrapolations of the spin gap $\Delta_{\rm T}$ on RCL-2L cylinders ($L = 4, 6, 8, 10$). For $J_2 < 0.5$, the data are fitted using the formula $\Delta_{\rm T}(L) = \Delta_{\rm T}(\infty)+\alpha/L^2+\beta/L^3+\gamma/L^4$, while for $J_2 \geq 0.5$, we fit the data using $\Delta_{\rm T}(L) = \Delta_{\rm T}(\infty)+a/L+b/L^2+c/L^4$. We estimate $\Delta_{\rm T}(\infty) = 0.018\pm0.01$ and 0.04 ± 0.01 for $J_2 = 0.5$ and 0.55, respectively.

energies of a "strong" red ("weak" blue) plaquette as E_s (E_w). Thus the plaquette DOP (pDOP) is defined as the difference of E_s and E_w, which is found to decay exponentially with a decay length $\xi_{\rm P}$. In Fig. 4(b), we examine the W_y dependence of the decay length $\xi_{\rm P}$ and observe a strong growth of $\xi_{\rm P}$ with W_y for $J_2 > 0.5$, consistent with the PVB state.

Spin gap and ground state energy.—We calculate spin gap $\Delta_{\rm T}$ on RCL-2L cylinders up to $L = 10$ following the method from Ref. [13]: We sweep the ground state first, and then target the $S = 1$ sector sweeping the middle $L \times L$ sites to avoid edge excitations. In Figs. 5(a) and 5(b), we show energies versus DMRG truncation error for RC10-20 cylinder at $J_2 = 0.5$ in the $S = 0$ and $S = 1$ sectors, respectively. In both plots, we have subtracted the ground-state energy $E_{\rm G} = -99.022(1)$ obtained through extrapolation keeping up to 36000 states as shown in Fig. 5(a). We find that we need about twice as many states to achieve the same energy error in the $S = 1$ sector as in the $S = 0$ sector. The difficulty to reach the convergence of the energy in the $S = 1$ sector may explain the overestimate of the spin gap in the earlier work Ref. [37]: We find $\Delta_{\rm T} \simeq 0.207$ while Ref. [37] estimates $\Delta_{\rm T} \simeq 0.248$. We obtain accurate spin gaps by keeping up to 36000 states at $L_y = 10$, which sets the limit of our simulations.

In Fig. 5(c), we show $\Delta_{\rm T}$ and the finite-size extrapolations (see additional extrapolated $\Delta_{\rm T}$ data in Fig. 1). In our fits, we find that $\Delta_{\rm T}$ extrapolates to zero for $J_2 \leq 0.48$, which is consistent with the Néel order for $J_2 \leq 0.44$ and suggests gapless spin excitations also for $0.44 < J_2 < 0.5$. For $J_2 = 0.5$ and 0.55, $\Delta_{\rm T}(L \to \infty)$ is fitted to 0.018 ± 0.01 and 0.04 ± 0.01, respectively; this is compatible with the VBC ordered phase with finite spin gap.

We have compared our DMRG ground-state energies on $L \times L$ tori to VMC results with additional Lanczos improvement steps from Ref. [41]. Since the torus system is extremely difficult to fully converge for 8×8 or larger sizes, we keep up to 32000 states and extrapolate the energy with the DMRG truncation error[52]. The extrapolated DMRG and Lanczos-VMC results are quite close to each other in the possible SL region $0.45 < J_2 < 0.5$ (see comparisons in Suppl. Material), indicating that the gapless Z_2 SL of Ref. [41] has very competitive energies in this region.

Summary and discussion.—We have studied the ground state of the spin-$\frac{1}{2}$ J_1-J_2 square lattice Heisenberg model by accurate $SU(2)$ DMRG simulations on cylinders with different geometries. We find that the Néel order persists up to $J_2 = 0.44$, while we find a nonmagnetic phase for $0.44 < J_2 < 0.6$. Contrary to the previous proposals of a possible gapped Z_2 SL from DMRG[37] or a gapless Z_2 SL from

VMC simulations[41], we establish the s-wave PVB order for $J_2 > 0.5$ by observing rapidly growing characteristic lengths of both the vertical and horizontal dimer orders on the RC systems, as well as the PVB order on the TC system. Between the Néel and PVB phases, we find a possible gapless SL for $0.44 < J_2 < 0.5$ as summarized in the phase diagram in Fig. 1. However, since the gapless SL region is small, it is also possible that the system has a deconfined quantum critical point in this region with larger length scale than the system width we can approach. We hope future studies can resolve these scenarios more clearly.

We would like to particularly thank H.-C. Jiang and L. Balents for extensive discussions. We also acknowledge stimulating discussions with K. S. D. Beach, Z.-C. Gu, W.-J. Hu, L. Wang, S. White, Z.-Y. Zhu, and A. Sandvik. This research is supported by the National Science Foundation through grants DMR-0906816 (S.S.G. and D.N.S.), DMR-1206096 (O.I.M.), DMR-1101912 (M.P.A.F.), the U.S. Department of Energy, Office of Basic Energy Sciences under grant No. DE-FG02-06ER46305 (W.Z), and by the Caltech Institute of Quantum Information and Matter, an NSF Physics Frontiers Center with support of the Gordon and Betty Moore Foundation (O.I.M. and M.P.A.F.).

[1] L. Balents, Nature **464**, 199 (2010).
[2] P. A. Lee, N. Nagaosa, and X. G. Wen, Rev. Mod. Phys. **78**, 17 (2006).
[3] R. Moessner and S. L. Sondhi, Phys. Rev. Lett. **86**, 1881 (2001).
[4] C. Nayak and K. Shtengel, Phys. Rev. B **64**, 064422 (2001).
[5] T. Senthil and O. Motrunich, Phys. Rev. B **66**, 205104 (2002).
[6] L. Balents, M. P. A. Fisher, and S. M. Girvin, Phys. Rev. B **65**, 224412 (2002).
[7] D. N. Sheng and L. Balents, Phys. Rev. Lett. **94**, 146805 (2005).
[8] S. V. Isakov, Y. B. Kim, and A. Paramekanti, Phys. Rev. Lett. **97**, 207204 (2006).
[9] S. V. Isakov, M. B. Hastings, R. G. Melko, Nature Physics **7**, 772 (2011).
[10] Y. C. He, D. N. Sheng, and Y. Chen, arxiv:1309.5669.
[11] A. Kitaev, Ann. Phys. (N.Y.) **321**, 2 (2006).
[12] H. C. Jiang, Z. Y. Weng, and D. N. Sheng, Phys. Rev. Lett. **101**, 117203 (2008).
[13] S. Yan, D. Huse, and S. R. White, Science **332**, 1173 (2011).
[14] S. Depenbrock, I. P. McCulloch, and U. Schollwöck, Phys. Rev. Lett. **109**, 067201 (2012).
[15] H. C. Jiang, Z. H. Wang, and L. Balents, Nature Physics **8**, 902 (2012).
[16] N. Read and S. Sachdev, Phys. Rev. Lett. **66**, 1773 (1991).
[17] X. G. Wen, Phys. Rev. B **44**, 2664 (1991).
[18] X. G. Wen, Phys. Rev. B **40**, 7387 (1989).
[19] L. Balents, M. P. A. Fisher, and C. Nayak, Phys. Rev. B **60**, 1654 (1999).
[20] T. Senthil and M.P.A. Fisher, Phys. Rev. B **62**, 7850 (2000); Phys. Rev. Lett. **86**, 292 (2001).
[21] S. Sachdev and R. Bhatt, Phys. Rev. B **41**, 9323 (1990).
[22] Andrey V. Chubukov and Th. Jolicoeur, Phys. Rev. B **44**, 12050 (1991).
[23] M. E. Zhitomirsky and K. Ueda, Phys. Rev. B **54**, 9007 (1996).
[24] A. E. Trumper, L. O. Manuel, C. J. Gazza, and H. A. Ceccatto, Phys. Rev. Lett. **78**, 2216 (1997).
[25] Rajiv R. P. Singh, W. H. Zheng, C. J. Hamer, and J. Oitmaa, Phys. Rev. B **60**, 7278 (1999).
[26] L. Capriotti and S. Sorella, Phys. Rev. Lett. **84**, 3173 (2000).
[27] L. Capriotti, F. Becca, A. Parola, and S. Sorella, Phys. Rev. Lett. **87**, 097201 (2001).
[28] G. M. Zhang, H. Hu, and L. Yu, Phys. Rev. Lett. **91**, 067201 (2003).
[29] K. Takano, Y. Kito, Y. One, and K. Sano, Phys. Rev. Lett. **91**, 197202 (2003).
[30] M. Mambrini, A. Läuchli, D. Poilblanc, and F. Mila, Phys. Rev. B **74**, 144422 (2006).
[31] R. Darradi, O. Derzhko, R. Zinke, J. Schulenburg, S. E. Krüger, and J. Richter, Phys. Rev. B **78**, 214415 (2008).
[32] L. Isaev, G. Ortiz, and J. Dukelsky, Phy. Rev. B **79**, 024409 (2009).
[33] J. Richter and J. Schulenburg, Eur. Phys. J. B **73**, 117 (2010).
[34] J. Reuther and P. Wölfle, Phys. Rev. B **81**, 144410 (2010).
[35] J. F. Yu, Y. J. Kao, Phys. Rev. B **85**, 094407 (2012).
[36] L. Wang, Z. C. Gu, F. Verstraete, and X. G. Wen, arxiv:1112.3331.
[37] H. C. Jiang, H. Yao, and L. Balents, Phys. Rev. B **86**, 024424 (2012).
[38] F. Mezzacapo, Phys. Rev. B **86**, 045115 (2012).
[39] T. Li, F. Becca, W. J. Hu, S. Sorella, Phys. Rev. B **86**, 075111 (2012).
[40] L. Wang, D. Poilblanc, Z. C. Gu, X. G. Wen, and F. Verstraete, Phys. Rev. Lett. **111**, 037202 (2013).
[41] W. J. Hu, F. Becca, A. Parola, and S. Sorella, Phys. Rev. B **88**, 060402 (2013).
[42] R. L. Doretto, arxiv:1309.6490.
[43] A. Kitaev, J. Preskill, Phys. Rev. Lett. **96**, 110404 (2006).
[44] M. Levin, X.-G. Wen, Phys. Rev. Lett. **96**, 110405 (2006).
[45] R. Ganesh, Jeroen van den Brink, and S. Nishimoto, Phys. Rev. Lett. **110**, 127203 (2013).
[46] Zhenyue Zhu, D. A. Huse, and S. R. White, Phys. Rev. Lett. **110**, 127205 (2013).
[47] S. S. Gong, D. N. Sheng, Olexei I. Motrunich, and Matthew P. A. Fisher, Phys. Rev. B **88**, 165138 (2013).
[48] T. Senthil, L. Balents, S. Sachdev, A. Vishwanath, and Matthew P. A. Fisher, Phys. Rev. B **70**, 144407 (2004).
[49] T. Senthil, A. Vishwanath, L. Balents, S. Sachdev, and Matthew P. A. Fisher, Science **303**, 1490 (2004).
[50] I. P. McCulloch and M. Gulácsi, Europhys. Lett. **57**, 852 (2002); I. P. McCulloch, J. Stat. Mech. **2007**, P10014 (2007).
[51] A. W. Sandvik, Phys. Rev. B **85**, 134407 (2012).
[52] We get much better convergence on cylinder than on torus. We can achieve truncation error 1×10^{-6} for $L_y = 10$ cylinder and 5×10^{-6} for $L_y = 12$ cylinder. For example, for $J_2 = 0.5$ and $L_y = 10$, we get truncation error 1×10^{-6} on cylinder by keeping 20000 states, while the error is much larger 8×10^{-5} on 10×10 torus even when we keep 32000 states.
[53] S. R. White and A. L. Chernyshev, Phys. Rev. Lett. **99**, 127004 (2007).
[54] We get converged m_s^2 for $L \leq 12$ by keeping more than 20000 states, while the results for $L = 14$ are obtained through extrapolations with the DMRG truncation error.
[55] A. W. Sandvik, Phys. Rev. Lett. **98**, 227202 (2007).
[56] R. G. Melko and R. K. Kaul, Phys. Rev. Lett. **100**, 017203 (2008).
[57] F. Jiang, M. Nyfeler, S. Chandrasekharan, and U. Wiese, J. Stat. Mech.: Theory and Experiment **2008** 02009 (2008).
[58] J. Lou, A. W. Sandvik, N. Kawashima, Phys. Rev. B **80**,

180414(R) (2009).
[59] J. Lou and A. W. Sandvik, Phys. Rev. B **80**, 212406 (2009).
[60] A. W. Sandvik, Phys. Rev. Lett. **104**, 177201 (2010).
[61] Matthew S. Block, R. G. Melko, R. K. Kaul, Phys. Rev. Lett. **111**, 137202 (2013).
[62] S. Pujari, K. Damle, and F. Alet, Phys. Rev. Lett. **111**, 087203 (2013).
[63] In $U(1)$ DMRG calculations for $L_y \geq 10$, one needs to extrapolate ξ_y with the DMRG truncation error, which may give some uncertainty to ξ_y.
[64] H. Yao and S. A. Kivelson, Phys. Rev. Lett. **108**, 247206 (2012).

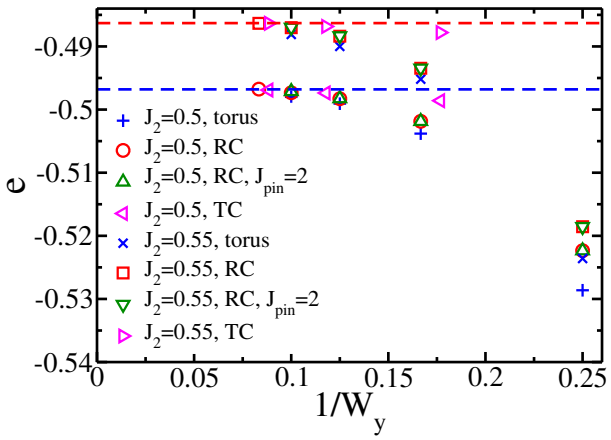

FIG. 6: (color online) DMRG ground-state energy per site for $J_2 = 0.5$ and 0.55 on torus, on RC cylinder without pinning or with vertical dimer boundary pinning $J_{\rm pin} = 2.0$ (see Fig. 1), as well as on TC cylinder (Fig. 4). The energies on torus are obtained through extrapolation with DMRG truncation error (see Table I). On cylinder, we get bulk energy by subtracting the energies of two long cylinders with different system lengths. With growing system width, the energies on different samples approach each other, giving the estimates of ground-state energy in the 2D limit for $J_2 = 0.5$ and 0.55 as $e_\infty \simeq -0.4968$ and -0.4863, respectively.

Supplementary Material

DMRG ground-state energies for $J_2 = 0.5$ and 0.55.—We show our DMRG ground-state energies for $J_2 = 0.5$ and 0.55 in Fig. 6. We study $L \times L$ torus systems with $L = 4, 6, 8, 10$. We keep more than $M = 32000$ optimal states for DMRG sweeping, and estimate the energy through extrapolation of finite-M energies via DMRG truncation error (see data in Table I below). For cylinders, we obtain bulk energy by subtracting the energies of two long cylinders with different system lengths to eliminate boundary effects.

As shown in Fig. 6, the energies per site of all samples increase slowly with increasing system width W_y and approach close to each other for $W_y \gtrsim 10$. The energies on torus are lower than those on cylinder, and the difference decreases with increasing W_y. The bulk energy on RC cylinder is essentially independent of the boundary pinning $J_{\rm pin}$. As the ground-state energy appears close to convergence for $W_y \geq 8$, we take a simple straight line fitting of the large-size results to give estimates of the energy in the 2D limit e_∞ as shown by the dashed lines in Fig. 6. We find $e_\infty \simeq -0.4968$ and -0.4863 for $J_2 = 0.5$ and 0.55, respectively.

Horizontal dimer order on RC cylinder without pinning.—On RC cylinder without pinning, the open edges break the lattice translation symmetry only in the x direction. The horizontal NN bond energies have the "strong-weak" dimer pattern as shown in Fig. 7(a). We define the hDOP as the difference of the adjacent horizontal NN bond energies, which decays exponentially with a decay length $\xi_{\rm x}$. In Fig. 7(b), we show the hDOP decay length $\xi_{\rm x}$ versus system width. For $J_2 < 0.5$,

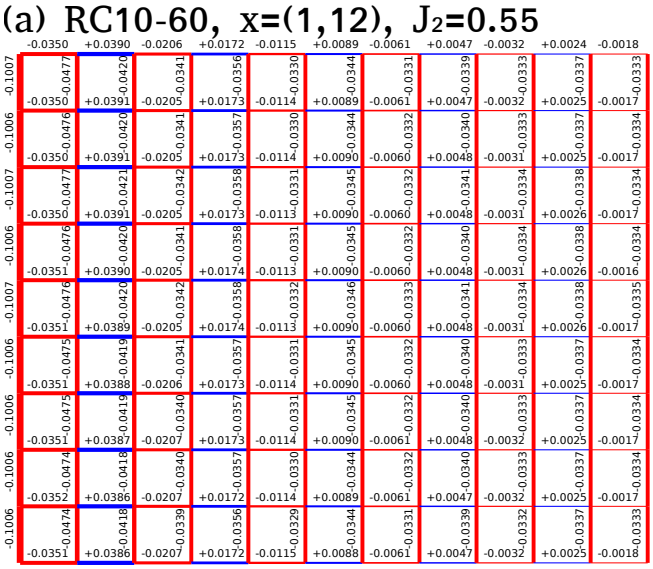

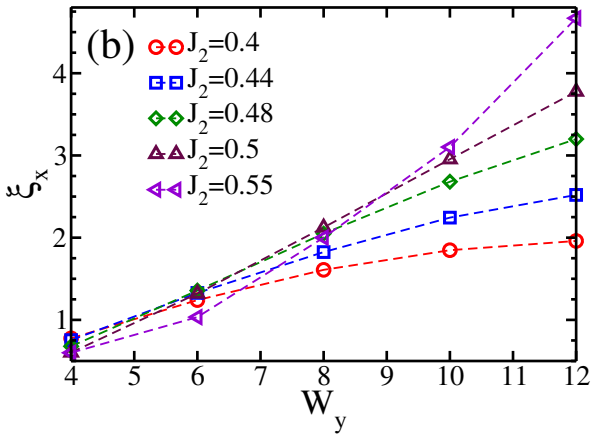

FIG. 7: (color online) (a) Subtracted NN bond energies for $J_2 = 0.55$ on RC10-60 cylinder without pinning; the subtracted number -0.2763 is the average horizontal bond energy in the bulk of the lattice. Here we show the left 12 columns. The alternation of red (negative number) and blue (positive number) bonds indicates horizontal dimer texture. (b) hDOP decay length $\xi_{\rm x}$ versus system width on RC cylinder without pinning. The extracted decay lengths $\xi_{\rm x}$ are similar to those in Fig. 3(c) obtained on RC cylinder with the vertical dimer pinning.

$\xi_{\rm x}$ grows more slowly than linearly and approaches saturation on large size, which is consistent with vanishing dimer order. However, for $J_2 > 0.5$, $\xi_{\rm x}$ grows fast, suggesting nonzero bulk hDOP on wider cylinders. This horizontal dimer order supports our claim of the VBC state for $J_2 > 0.5$. We also find that the $\xi_{\rm x}$ obtained here are almost the same as those in Fig. 3(c) where the cylinder systems have the vertical bond pinning.

Pinning independence of the vDOP decay length $\xi_{\rm y}$.— In the main text, we introduced modified vertical bonds $J_{\rm pin}$ on boundaries to break the lattice translational symmetry in the

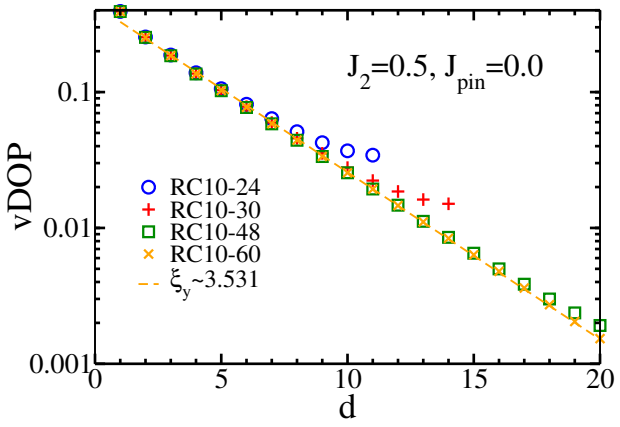

FIG. 8: (color online) Log-linear plot of the vDOP on RC10 cylinders with different system lengths at $J_2 = 0.5$ and $J_{\rm pin} = 0.0$. The exponential fitting gives decay length $\xi_{\rm y} = 3.531$.

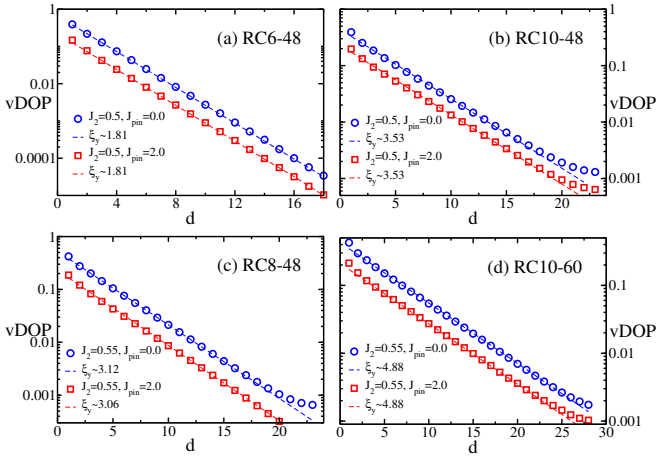

FIG. 9: (color online) Comparisons of the vDOP textures on RC cylinder with different boundary pinnings. We have studied several different $J_{\rm pin}$ and found that although the vDOP varies with $J_{\rm pin}$, the decay length $\xi_{\rm y}$ is almost independent of the pinning strength. Here we show the results with $J_{\rm pin} = 0.0$ and 2.0.

y direction, allowing us to study the vDOP and the width dependence of the vDOP decay length. A direct question is whether the pinning strength affects these quantities. We have compared the vDOP and its decay length for several different pinning strengths, from weak pinning $J_{\rm pin} = 1.01, 1.1, 1.2$ to strong pinning $J_{\rm pin} = 2.0$ and $J_{\rm pin} = 0.0$. First of all, in Fig. 8 we show that our results are obtained on quite long cylinders, thus minimizing the influence of finite-size effects on the decay length. Next, in Fig. 9 we show some examples of varying boundary pinning at $J_2 = 0.5, 0.55$; we find that although the amplitude of the vDOP texture varies with $J_{\rm pin}$, the decay length $\xi_{\rm y}$ is almost independent of the pinning strength, indicating that our results with pinning are robust properties of the bulk (infinitely long cylinder) phase.

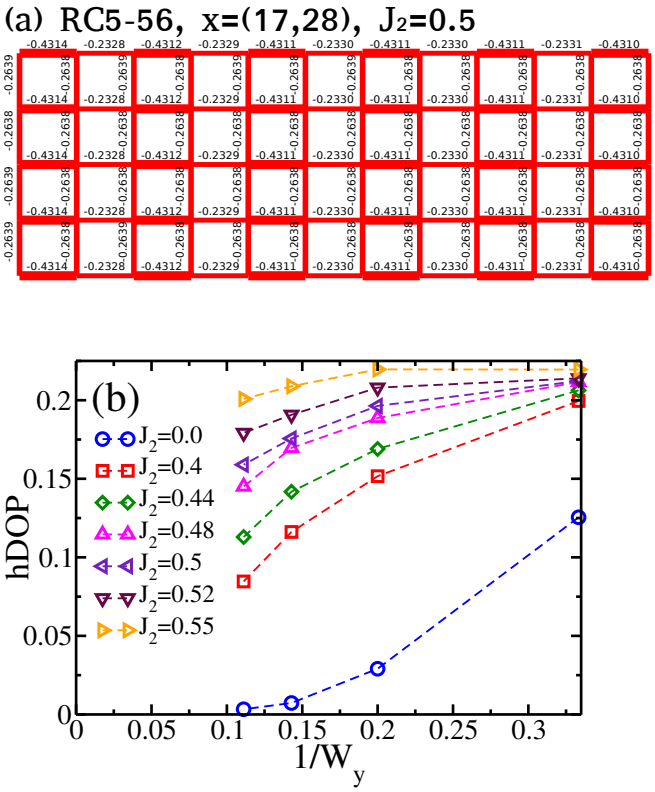

FIG. 10: (color online) (a) The NN bond energies for RC5-56 cylinder at $J_2 = 0.5$, showing bonds with x from 17 to 28. The system has a spontaneous bulk horizontal dimer order, and the bulk hDOP is defined as the difference of the strong and weak bond energies in the middle of cylinder. (b) Width dependence of the hDOP on the odd-L_y RC cylinders, showing the data for $W_y = 3, 5, 7, 9$.

Horizontal dimer order on RC cylinder with odd L_y.—On finite-size odd-L_y RC cylinder, the system spontaneously develops a nonzero horizontal dimer order in the bulk, which happens both when the 2D phase is VBC or Z_2 SL[37, 64]. For a Z_2 SL in the 2D limit, the dimer order would decay exponentially with growing L_y. On the other hand, for a VBC state, it should go to a finite value in the 2D limit[37, 64]. We study the horizontal dimer order on odd-L_y RC cylinder with L_y up to 9 and L_x up to 100 to get the results representing $L_x \to \infty$ cylinders. We define the absolute difference of the strong and weak horizontal bond energies in the bulk as hDOP, see Fig. 10(a). We show thus measured hDOP versus $1/W_y$ in Fig. 10(b). For $J_2 < 0.5$ the hDOP decays fast with the cylinder width and appears to extrapolate to zero, while for $J_2 > 0.5$ the hDOP has a slow decay and seems to saturate to a finite value. The nonzero hDOP does not support a Z_2 SL, but indicates a VBC state for $J_2 > 0.5$.

Dimer structure factors on RC cylinder.— The CVB order breaks rotational symmetry, while the PVB order preserves it. Following Ref. [30], we consider two structure factors $S_{\rm vbc}$ and $S_{\rm col}$ obtained from the dimer-dimer correlations. $S_{\rm vbc}$ diverges in both the CVB and PVB states, while $S_{\rm col}$ diverges

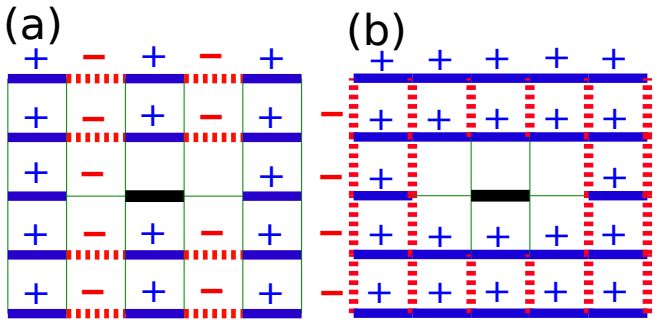

FIG. 11: (color online) Phase factors $\varepsilon_\lambda(k,l)$ for (a) "vbc" and (b) "col" dimer structure factors defined in Eq. (2). The solid bonds have phase factor $\varepsilon_\lambda(k,l) = 1$, while dashed bonds have $\varepsilon_\lambda(k,l) = -1$. The (k,l) bonds that are nearest neighbors to the reference bond (i,j) (central black solid bond) are omitted in the calculation of the structure factors.

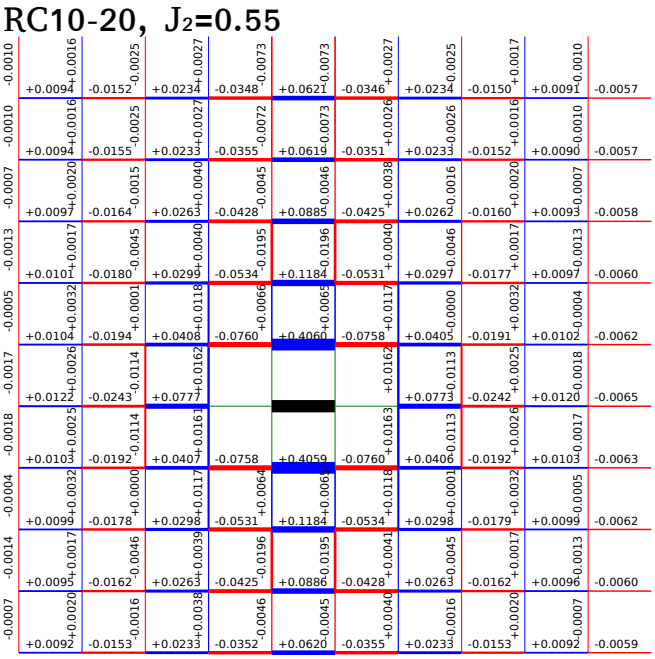

FIG. 12: (color online) Dimer-dimer correlation function for $J_2 = 0.55$ on RC10-20 cylinder. The black bond in the middle of the cylinder denotes the reference bond (i,j). The blue and red bonds indicate the positive and negative correlations, respectively. Here the middle 10×10 lattice dimer correlations are shown, which are used to calculate the dimer structure factors.

only in the CVB state. The structure factors are defined as

$$S_\lambda = \sum_{(k,l)} \varepsilon_\lambda(k,l) C_{ijkl}, \tag{2}$$

where λ is either "vbc" or "col". The phase factors $\varepsilon_\lambda(k,l)$ are shown in Fig. 11, which reproduces Fig. 7 in Ref. [30]. Dimer-dimer correlation function C_{ijkl} is defined as

$$C_{ijkl} = 4\left[\langle (S_i \cdot S_j)(S_k \cdot S_l)\rangle - \langle S_i \cdot S_j\rangle \langle S_k \cdot S_l\rangle\right]. \tag{3}$$

We calculate dimer-dimer correlation function on the RCL-

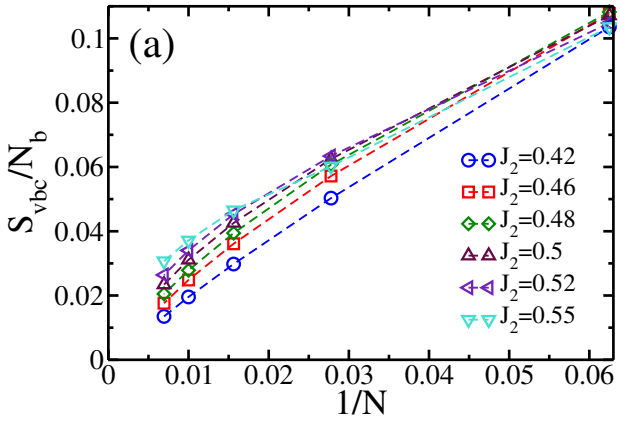

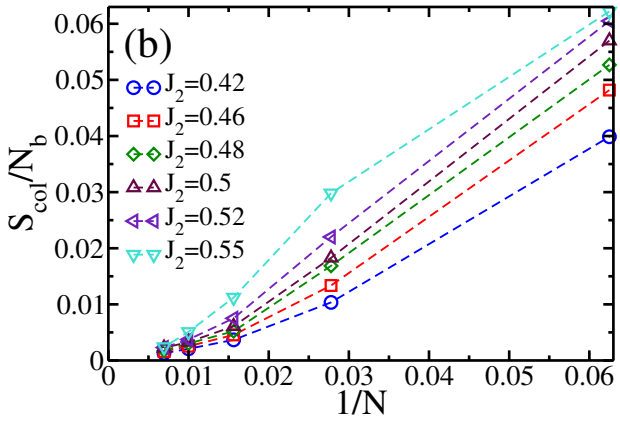

FIG. 13: (color online) Size dependence of dimer structure factors (a) $S_{\rm vbc}/N_b$ and (b) $S_{\rm col}/N_b$. $S_{\rm vbc}/N_b$ appears to extrapolate to finite values for $J_2 > 0.5$, while $S_{\rm col}/N_b$ decays quite fast and approaches zero with increasing system size thus excluding the CVB order. This suggests the PVB order for $J_2 > 0.5$.

$2L$ cylinder with a reference bond (i,j) in the middle of the cylinder (we have considered both horizontal and vertical reference bonds but will show only the former). Figure 12 shows the dimer-dimer correlations on the RC10-20 cylinder at $J_2 = 0.55$ with the reference bond (i,j) oriented horizontally in the middle of the cylinder. The red and blue bonds indicate negative and positive dimer correlations, respectively. We see alternating red and blue horizontal bonds of comparable strengths, while the vertical bonds show significantly weaker correlations; this picture looks much more like the pattern of the pure s-wave plaquette state (PVB) in Table III of Ref. [30] rather than the pattern of the pure columnar state.

Figure 13 shows the structure factors $S_{\rm vbc}/N_b$ and $S_{\rm col}/N_b$ obtained with a horizontal reference bond (i,j) and normalized by the number of bonds N_b used to calculate the structure factors. In Fig. 13(a), we see that $S_{\rm vbc}/N_b$ approaches zero for $J_2 < 0.5$ and possibly extrapolates to finite values

for $J_2 > 0.5$ if we fit the large-size data using polynomials of $1/N$. This suggests PVB or CVB orders at $J_2 > 0.5$. In Fig. 13(b), we see that $S_{\rm col}/N_b$ decays quite fast with system size and always approaches zero in the thermodynamic limit, which implies vanishing CVB order. Thus, the behavior of these two structure factors reveals the possible PVB order at $J_2 > 0.5$ and clearly excludes the CVB order. We observe similar results with a vertical reference bond (i, j) (not shown).

We also notice that when we plot $S_{\rm vbc}/N_b$ versus $1/L$ ($L = \sqrt{N}$), the data could be extrapolated to zero or small values also for $J_2 > 0.5$, which would be similar to the analysis in Ref. [37]. However, for $J_2 = 0.55$, the extrapolation function to zero is almost linear in $1/L$ (plot not shown), while in a phase with no VBC order we would expect $S_{\rm vbc}/N_b$ to vanish as $1/N \sim 1/L^2$. Thus this data is not consistent with vanishing VBC order.

Comparisons of torus energies from DMRG and VMC.— Table I shows energy comparisons of DMRG and VMC for $J_2 = 0.4, 0.45, 0.5$, and 0.55; it includes DMRG results obtained by keeping 4096, 6144, and 8192 $SU(2)$ states [equivalent to about 16000, 24000, and 32000 $U(1)$ optimal states], as well as VMC results with Lanczos improvement steps from Ref. [41]. DMRG (∞) denotes the DMRG energy extrapolated with truncation error; as illustrated in Fig. 14, we extrapolate the data points using a straight line fitting. VMC (p=∞) denotes the VMC energy extrapolations with the variance in Ref. [41]. The overall agreement shows, on one hand, that the DMRG is performing reasonably well even in the most challenging torus geometry. Here we emphasize that all results in the main text are obtained using cylinder geometry where the DMRG measurements are much better converged[52] and represent essentially exact unbiased measurements. On the other hand, the excellent performance of the Lanczos-VMC method is also notable. It would be interesting to see this method tried in the cylinder geometries and results subjected to the finite-size scaling analysis as in the present work.

Entanglement entropy.—For gapped quantum states with topological order, topological entanglement entropy (TEE) γ is proposed to characterize non-local feature of entanglement[43, 44]. The Renyi entropies of a subsystem A with reduced density matrix ρ_A are defined as $S_n = (1-n)^{-1}\ln({\rm Tr}\rho_A^n)$; $n \to 1$ limit gives the Von Neuman entropy. For a topologically ordered state, Renyi entropies have the form $S_n = \alpha L - \gamma$, where L is the boundary of the subsystem, and all other terms vanish in the large L limit; α is a non-universal constant, while a positive γ is a correction to the area law of entanglement and reaches a universal value determined by total quantum dimension D of quasiparticle excitations[43, 44]. Previous DMRG study[37] found $\gamma \approx \ln 2$ in the intermediate region of J_2 consistent with a Z_2 SL for this model. We compute the entanglement entropy (EE) on long cylinders by partitioning the system in the middle along the vertical direction. For each fixed L_y, we fit the entropy to $L_x \to \infty$ limit to find the entropy of a possible minimum entropy state[15].

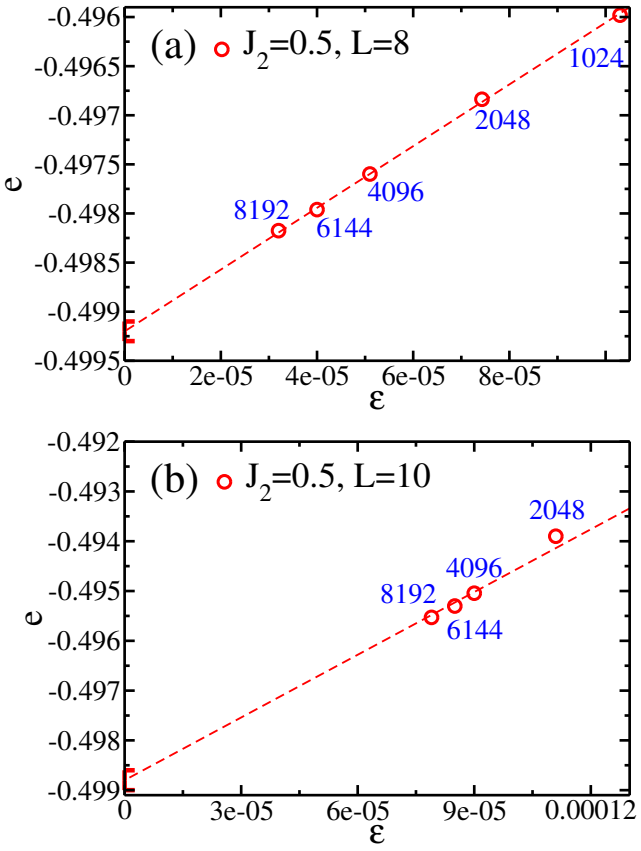

FIG. 14: (color online) Ground-state energy per site e versus DMRG truncation error ε on the $L\times L$ torus systems for (a) $J_2 = 0.5$, $L = 8$, and (b) $J_2 = 0.5$, $L = 10$. The numbers in the figures denote the kept $SU(2)$ states M for obtaining the energy. We extrapolate the data with a straight line fitting and denote the $\varepsilon \to 0$ intercept (corresponding to $M \to \infty$) as DMRG (∞).

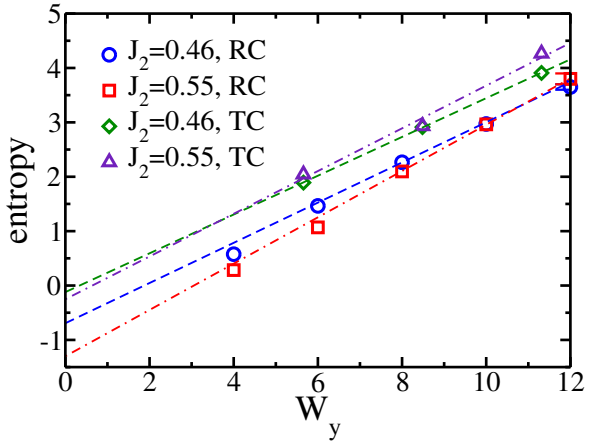

FIG. 15: (color online) Entanglement entropy as a function of system width on RC and TC cylinders. For each width, we obtain the entropy by extrapolating measurements on long cylinders to $L_x \to \infty$ limit.

$J_2 = 0.40$	DMRG (4096)	DMRG (6144)	DMRG (8192)	DMRG (∞)	VMC ($p = 0$)	VMC ($p = 1$)	VMC ($p = 2$)	VMC ($p = \infty$)
$L = 6$	-0.529734	-0.529742	-0.529744	$-0.529747(1)$	$-0.52715(1)$	$-0.52928(1)$	$-0.52957(1)$	$-0.52972(1)$
$L = 8$	-0.524648	-0.525013	-0.525196	$-0.5262(1)$	$-0.52302(1)$	$-0.52501(1)$	$-0.52539(1)$	$-0.52556(1)$
$L = 10$	-0.521487	-0.522043	-0.522391	$-0.5253(2)$	$-0.52188(1)$	$-0.52368(1)$	$-0.5240(1)$	$-0.52429(2)$
$J_2 = 0.45$	DMRG (4096)	DMRG (6144)	DMRG (8192)	DMRG (∞)	VMC ($p = 0$)	VMC ($p = 1$)	VMC ($p = 2$)	VMC ($p = \infty$)
$L = 6$	-0.515637	-0.515652	-0.515655	$-0.515660(1)$	$-0.51364(1)$	$-0.51538(1)$	$-0.51558(1)$	$-0.51566(1)$
$L = 8$	-0.510162	-0.510534	-0.510740	$-0.5116(1)$	$-0.50930(1)$	$-0.51101(1)$	$-0.51125(1)$	$-0.51140(1)$
$L = 10$	-0.507193	-0.507677	-0.507976	$-0.5110(3)$	$-0.50811(1)$	$-0.50973(1)$	$-0.51001(1)$	$-0.51017(2)$
$J_2 = 0.50$	DMRG (4096)	DMRG (6144)	DMRG (8192)	DMRG (∞)	VMC ($p = 0$)	VMC ($p = 1$)	VMC ($p = 2$)	VMC ($p = \infty$)
$L = 6$	-0.503771	-0.503797	-0.503805	$-0.503808(1)$	$-0.50117(1)$	$-0.50323(1)$	$-0.50357(1)$	$-0.50382(1)$
$L = 8$	-0.497598	-0.497961	-0.498175	$-0.4992(1)$	$-0.49656(1)$	$-0.49855(1)$	$-0.49886(1)$	$-0.49906(1)$
$L = 10$	-0.495044	-0.495301	-0.495530	$-0.4988(2)$	$-0.49521(1)$	$-0.49718(1)$	$-0.49755(1)$	$-0.49781(2)$
$J_2 = 0.55$	DMRG (4096)	DMRG (6144)	DMRG (8192)	DMRG (∞)	VMC ($p = 0$)	VMC ($p = 1$)	VMC ($p = 2$)	VMC ($p = \infty$)
$L = 6$	-0.495096	-0.495150	-0.495167	$-0.495186(1)$	$-0.48992(1)$	$-0.49303(1)$	$-0.49399(1)$	$-0.49521(7)$
$L = 8$	-0.487685	-0.487982	-0.488160	$-0.4891(1)$	$-0.48487(1)$	$-0.48777(1)$	$-0.48841(2)$	$-0.48894(3)$
$L = 10$	-0.484890	-0.485239	-0.485434	$-0.4880(2)$	$-0.48335(1)$	$-0.48622(1)$	$-0.48693(3)$	$-0.48766(6)$

TABLE I: DMRG and VMC ground-state energies on $L \times L$ tori with $J_2 = 0.4, 0.45, 0.5$ and 0.55. DMRG energies are obtained by keeping 4096, 6144, and 8192 $SU(2)$ states. DMRG (∞) is obtained from the straight line energy extrapolation with DMRG truncation error as illustrated in Fig. 14. The VMC energies are from Ref. [41]; p denotes the Lanczos step; and VMC ($p = \infty$) is obtained from extrapolation with the variance.

In Fig. 15, we show our DMRG results for the EE at $J_2 = 0.46$ and 0.55 on both TC and RC cylinders. We obtain accurate EE when $W_y < 12$. For $W_y = 12$, we extrapolate the EE with the DMRG truncation error, which has significant uncertainty from the extrapolation. On RC cylinder, we perform linear fit of the EE versus W_y using the three largest sizes. We find the TEE at $J_2 = 0.46$ is close to $\ln 2$, while at $J_2 = 0.55$ is close to -1.3. However, the system appears to have large finite-size effects, which can be seen by comparing the results on the RC and TC cylinders. On the TC cylinder, the linear fits of the EE vs W_y give the TEE close to zero, which is different from the RC cylinder. Similar effect has also been observed in the J_1-J_2 model on the honeycomb lattice[46, 47]. Because of such strong finite-size effects, the TEE obtained by fitting EE on our small sizes may not be able to distinguish different quantum phases in the J_1-J_2 square lattice model.